



Influencing Factors and Process Optimization of Al/SiC Powder-cored Wires by Plasma Transferred Wire Arc Spraying

Ming Liu¹ · Qi-qing Peng³ · Yan-fei Huang¹ · Ping-hua Li⁴ · Guo-long Tan⁵ · Xuan-ping Luo³ · Qian-sen Qiao⁶ · Hai-dou Wang^{1,2} · Wei Lang³

Submitted: 11 January 2024 / in revised form: 18 May 2024 / Accepted: 27 June 2024
© ASM International 2024

Abstract Wire thermal spraying, one of the significant coating preparation technologies in the field of thermal spraying, has the advantages of low cost, high material utilization rate and fast coating deposition. Powder-cored wires, with easily controllable compositions, are used as spraying materials to prepare functional coatings with special properties. Coatings prepared by traditional wire thermal spraying technologies, mainly including wire flame spraying (WFS), wire arc spraying (WAS) and plasma wire spraying, have some defects, such as weak bonding strength and high porosity. In this paper, the plasma transferred wire arc spraying (PTWAS) technology was innovatively proposed, by which Al/SiC powder-cored wires were successfully sprayed to deposit the aluminum (Al)/Nicalon (SiC) composite coating. Furthermore, the influences of spraying current (I), argon (Ar) flow rate (L_{Ar}), hydrogen (H_2) flow rate (L_{H_2}) and other factors on Al/SiC powder-cored wires prepared by PTWAS and the optimization of the coating preparation process were mainly studied *via* the single factor method and the response surface methodology. After experimental

exploration and analysis, the optimized process parameters were finally determined as follows: L_{Ar} was 120 L min^{-1} , I was 160 A, L_{H_2} was 5 L min^{-1} , the spraying distance was 100 mm, the wire feeding speed (V) was 0.18 m s^{-1} , and the distance between the wire and nozzle (d) was 10 mm. It was found in the test that the porosity of the optimized Al/SiC composite coating was only 1.6%, the average microhardness was 102 HV_{0.1}, and the average bonding strength was 36.5 MPa. The comprehensive properties of this coating were better than those of the Al/SiC composite coatings prepared by WFS and WAS.

Keywords Al/SiC powder-cored wire · plasma transferred wire arc spraying · porosity · response surface methodology · wire thermal spraying technology

Introduction

Thermal spraying technology is commonly used to prepare coatings in the field of surface engineering. With flame, arc and plasma arc as heat sources, this technology can be used to instantaneously heat spraying materials (powder, wire, bar, *etc.*) into molten or semi-molten particles in the high-temperature and high-speed flame flow, which impact the pre-treated substrate surface at a high speed, contributing to the formation of protective coatings with certain functions through the spreading, cooling and continuous overlapping and stacking of particles (Ref 1, 2). According to the state of spraying materials, thermal spraying technology can be classified into powder thermal spraying technology and wire thermal spraying technology. Among them, wire thermal spraying technology has the advantages of low cost, high material utilization rate and fast coating deposition, which can be used to prepare protective coatings on

✉ Qi-qing Peng
1371090419@qq.com

¹ National Key Laboratory for Remanufacturing, Army Academy of Armored Forces, Beijing 100072, China

² National Engineering Research Center for Remanufacturing, Army Academy of Armored Forces, Beijing 100072, China

³ PLA 77626 Force, Lasa, China

⁴ PLA 32144 Force, Weinan, China

⁵ State Key Laboratory of Metal Material Strength, Xi'an Jiaotong University, Xi'an 710049, China

⁶ PLA 96885 Force, Henan, China

the surface of large parts and components. It is mostly used to prepare metal and metal matrix composite coatings, mainly including wire flame spraying (WFS) (Ref 3-7), wire arc spraying (WAS) (Ref 8-12) and plasma wire spraying (PWS) (Ref 13-15).

Powder-cored wire is one of the spraying materials used in the wire thermal spraying technology. It is made of solid wire as the strip coating filler powder (Ref 16, 17). Its filler powder can be various metal, non-metallic and ceramic materials, with the characteristics of easy composition control, and can be used to prepare multi-functional composite coatings (Ref 18-21).

For plasma wire spraying, the key factors affecting the melting behavior of the metal wire and the quality of the coating mainly include spraying current, argon gas flow rate, hydrogen gas flow rate, and the distance between the wire and the nozzle (Ref 22-26). For example, Kharlamov (Ref 22) used mathematical models to scientifically calculate the relationship between wire melting behavior, wire feeding speed, and spraying current during plasma wire spraying, including: firstly, the formation of a metal jet (wire feeding speed of 5-7 m/min, spraying current of 200A); The second is to form almost identical sized droplets (with a wire feeding speed of 8-12 m/min); The third is to form droplets with significant differences in size (wire feeding speed of 12-15 m/min).

As we all know, Al-based coating is the most economical anti-corrosion coating in the marine environment, which can achieve corrosion protection of metal substrate (Ref 27, 28). However, the corrosion of marine structures usually coincides with wear, which accelerates the corrosion of coatings (Ref 29, 30) and reduces service life. Faced with the above-mentioned problems, research has shown that Nicalon (SiC) particle-reinforced Al-based composites are characterized by low density, high strength, excellent wear resistance and low cost, making themselves ideal metal-based composites with wear resistance and corrosion resistance (Ref 31-33).

In this paper, the plasma transferred wire spraying (PTWS) technology was innovatively put forward, and the Al/SiC cored wire was used as the spraying material to successfully prepare the Al/SiC composite coating with low porosity, high bonding strength and excellent comprehensive performance. The single factor method and response surface method were used to explore the influence factors and process optimization of plasma transferred arc spraying of Al/SiC cored wire.

Experimental Procedure

Experimental Materials

In this research, the experimental materials mainly included substrates and spraying materials. To be specific, the 304 stainless steel was used as the substrate; its main compositions are shown in Table 1. The steel was cut into blocks of $50 \times 10 \times 2$ mm according to the experimental requirements.

The spraying material used in the experiment is Al/SiC cored wire with a diameter of 2 mm, which was customized by the research team to Beijing Yanbang New Materials Technology Co., Ltd. according to experimental research needs. The filling rate of SiC particles is 30%, with a particle size of 10-60 μm and a purity greater than 99.9%. The original morphology is shown in Fig. 1. The production process and physical images of Al/SiC cored wire are shown in Fig. 2.

Substrate Pretreatment

The impurities such as oil stains on the substrate surface were ultrasonically cleaned with alcohol before spraying, and then, sandblasting pre-treatment was performed on the substrate surface through the process shown in Table 2 to further remove the impurities and increase the roughness and activity of the substrate surface, thereby enhancing the bonding strength between the coating and the substrate.

PTWAS System

After substrate pre-treatment, Al/SiC powder-cored wires were sprayed through the PTWAS system at room temperature to prepare coatings. It is worth noting that PTWAS is a new wire spraying technology innovatively designed by the research group, which has not been publicly reported, so the system is explained as follows: The composition and working principle of the PTWAS system are shown in Fig. 3(a) and (b).

In this system, two power sources are used, with the small power source anode connected to the nozzle and the cathode connected to the tungsten electrode, mainly to generate a non-transfer arc inside the nozzle (Fig. 4a); the anode of the power supply is connected to the external wire, while the cathode is still connected to the tungsten electrode. The main purpose is to lead out the non-transfer

Table 1 Chemical composition of 304 stainless steel substrate

Element	C	Mn	P	S	Si	Cr	Ni	N	Cu
Content, wt. %	0.043	1.06	0.02	0.003	0.43	18.14	8.01	0.050	0.08

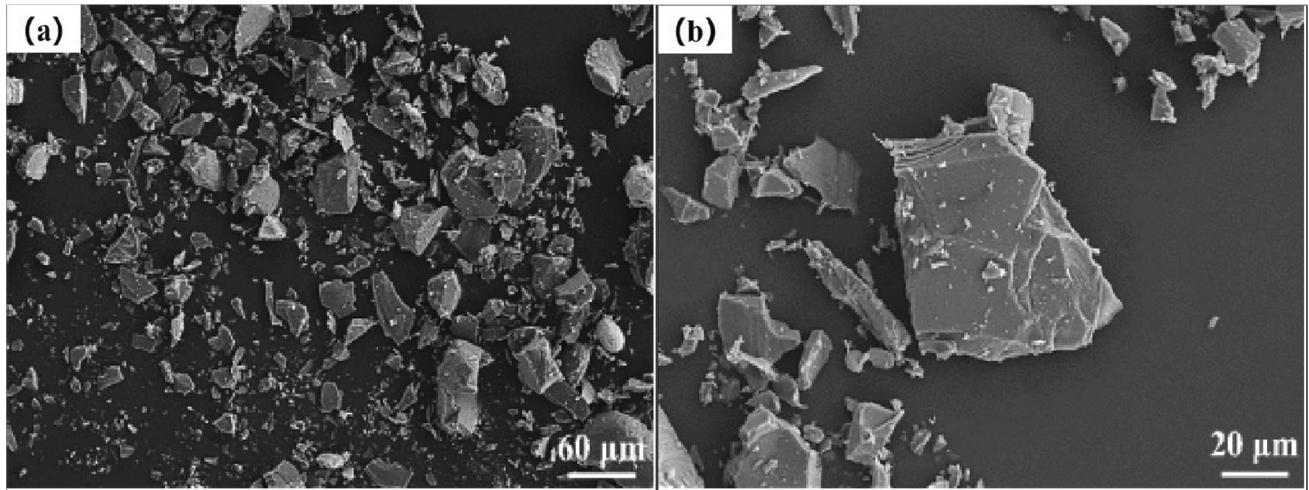


Fig. 1 Original morphology of SiC particles: (a) micromorphology of SiC particles; (b) SiC particle morphology at high magnification

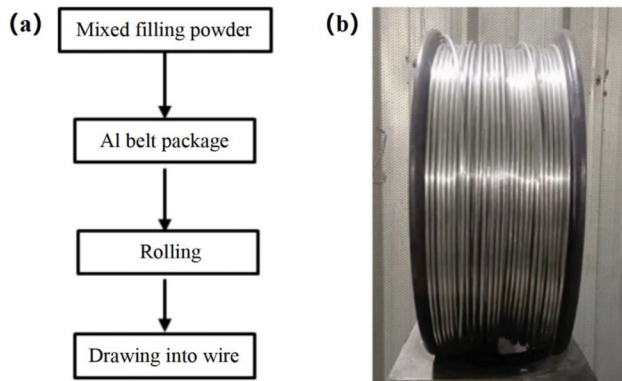


Fig. 2 (a) Production process of cored wire; (b) aluminum-based cored wire

Table 2 Process parameters of matrix sandblasting pretreatment

Sand blasting process	Parameter
Sand grain type	Al ₂ O ₃
Sand grain size	0.5 mm
Sand blasting pressure	0.4-0.6 MPa
Blasting distance	400 mm

arc inside the nozzle and form a transfer arc outside the nozzle (Fig. 4b).

It should be noted that the supersonic high-energy plasma transfer arc wire spraying system used in this article

has the following advantages compared to traditional plasma wire spraying systems:

- (1) The supersonic high-energy plasma transfer arc wire spraying system is based on the supersonic plasma powder spraying system. The nozzle adopts the classic Laval nozzle, so 80% of the transfer arc is still a compressed arc. Therefore, the arc still has the characteristics of high temperature and fast speed. Under the action of the Laval hole inside the nozzle, supersonic spraying can be achieved.
- (2) The anode nozzle of the supersonic high-energy plasma transfer arc wire spraying system is designed with a water circulation cooling system (traditional plasma wire spraying systems use air cooling (Ref 22, 23)), which can achieve a significant increase in spraying power. After testing, the spraying power of the system can now reach 72.5 kw (working current can reach 500A, while the working current of traditional plasma wire spraying systems is about 160-300A (Ref 22-26)). Figure 5 shows the jet morphology under different experimental parameters during the experimental testing of the supersonic high-energy plasma transfer arc wire spraying system.
- (3) The supersonic high-energy plasma transfer arc wire spraying system has the characteristics of a supersonic high-energy plasma powder spraying system, which can achieve synchronous transportation and

Fig. 3 (a) Schematic diagram of the plasma transfer arc spraying system; (b) schematic diagram of working principle of the system

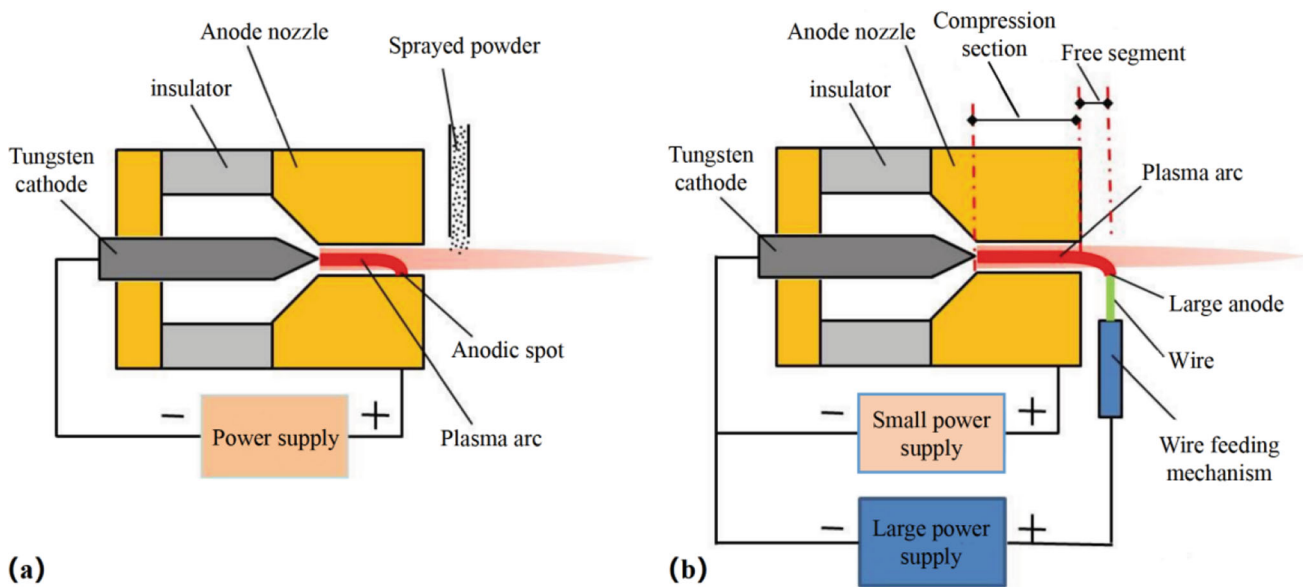
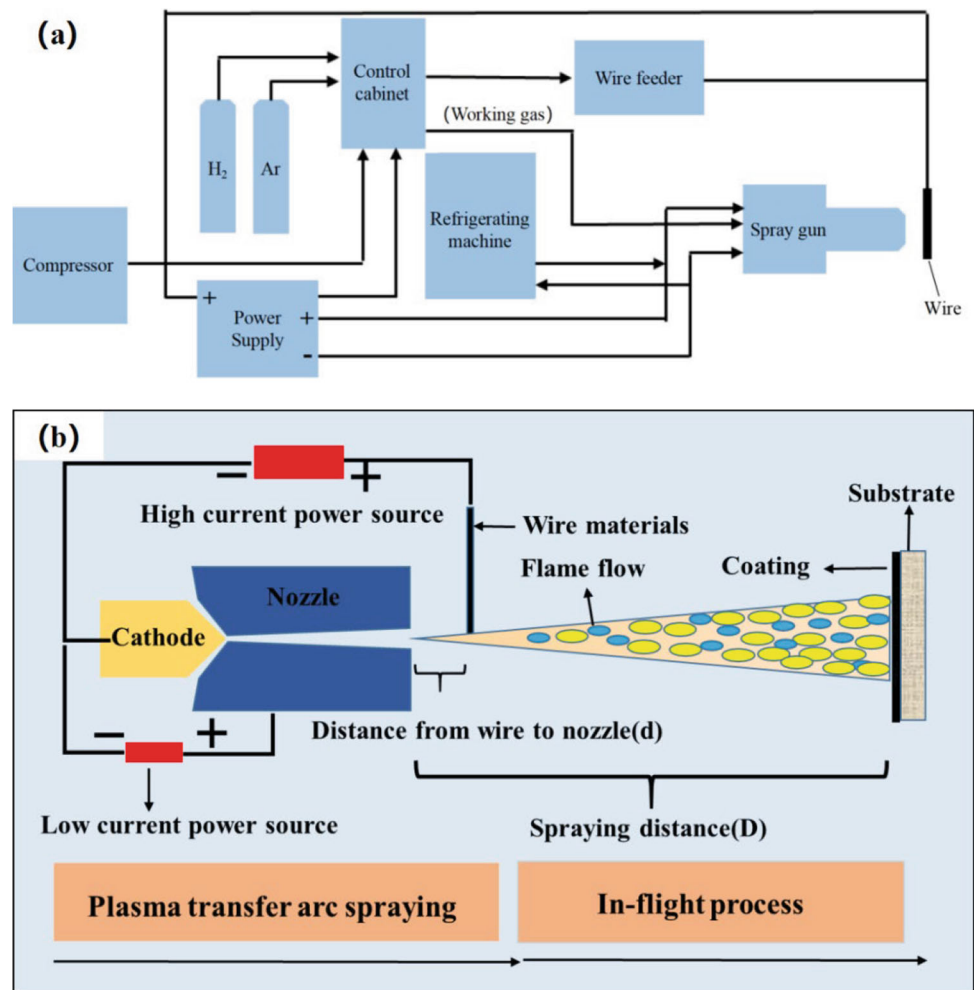


Fig. 4 Schematic diagram of non-transferable plasma powder spraying and transferable plasma wire spraying: (a) non-transferable plasma arc; (b) transfer plasma arc

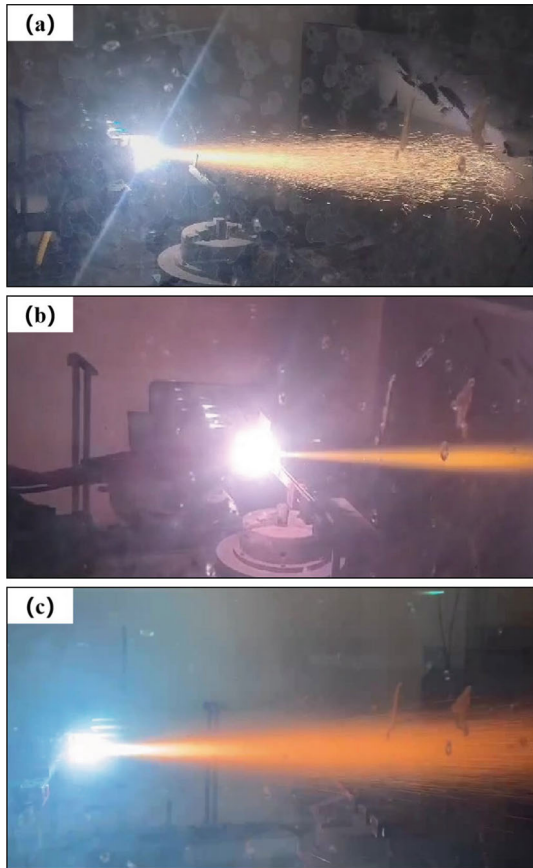


Fig. 5 Jet morphology during experimental testing of supersonic high-energy plasma transfer arc wire spraying system: (a) The silk material is Ni625, Spray current is 320A, spray voltage is 110 V, and spray power is 35.2KW; (b)The wire material is Fe based amorphous powder-cored wire material, the spraying current is 500A, the spraying voltage is 117 V, and the spraying power is 58.54KW; (c) The silk material is pure Al silk, the spraying current is 500A, the spraying voltage is 145 V, and the spraying power is 72.5KW

full melting of two forms of raw materials: internal powder feeding, external wire feeding, high melting point ceramic powder and metal wire; Compared with direct spraying of ceramic powder-cored wire, ceramic powder melts more fully, which can achieve the preparation of high-quality metal ceramic composite coatings and effectively improve the tribological properties of the coatings.

In summary, PTWAS, characterized by high spraying efficiency, low cost and good coating performance, is a coating preparation technology with spraying cost and efficiency similar to that of WAS and better coating performance, so it has significant application prospects in the high-efficiency and large-area equipment surface protection.

Microstructure Characterization of Composite Coatings

A high-resolution field emission scanning electron microscope (SEM, SU3500, Shanghai, China) equipped with an x-ray energy-dispersive spectrometer (EDS) was used to observe the micro-morphology of the surface and cross section of the coatings. Then, the image processing software ImageJ was employed to calculate the average porosity of the coatings through the grey level method.

In addition, the velocity and molten state of flying droplets were determined by the jet divergence and brightness observed from a macroscopic perspective since the molten state of spraying materials depended on the temperature of the plasma transferred arc.

Mechanical Property Test of Composite Coatings

The bonding strength of the coatings (Fig. 6a) was tested by a universal testing machine (MTS Exceed E45, China) according to GB/T8642-2002. During the test, only when the coatings were completely or uniformly peeled off could the test data be valid, and the average value of 5 sets of valid data was taken as the effective bonding strength. Then, the hardness test on the cross sections of the composite coatings was conducted *via* the Vickers hardness tester (MICROMET-6030, Buehler, Germany) by the “1”-shaped path method (Fig. 6b), and the average value was obtained by measuring 10 points.

Influencing Factors of PTWAS Jet

The relationship between various factors and PTWAS jet states (Fig. 7) revealed that the main factors influencing PTWAS included argon (Ar) flow rate (L_{Ar}), hydrogen (H_2) flow rate (L_{H_2}), the distance between wire and nozzle (d), spraying current (I) and spraying voltage (U).

- (1) Ar, the main working gas, on the one hand, provides heat after ionization. On the other hand, it accelerates the atomized droplets. Therefore, a larger L_{Ar} contributes to a higher droplet speed. L_{Ar} should not be too large because Ar will cool the droplets while accelerating them, so an excessive L_{Ar} will lead to the droplets cooling at an extremely high speed and affect their spreading effect on the substrates.
- (2) H_2 , an auxiliary gas, mainly provides heat to fully melt the wires, so it principally influences the temperature of droplets and U .
- (3) d mainly influences U and further affects the spraying power.

Fig. 6 Mechanical property test: (a) bonding strength test principle; (b) coating hardness test path

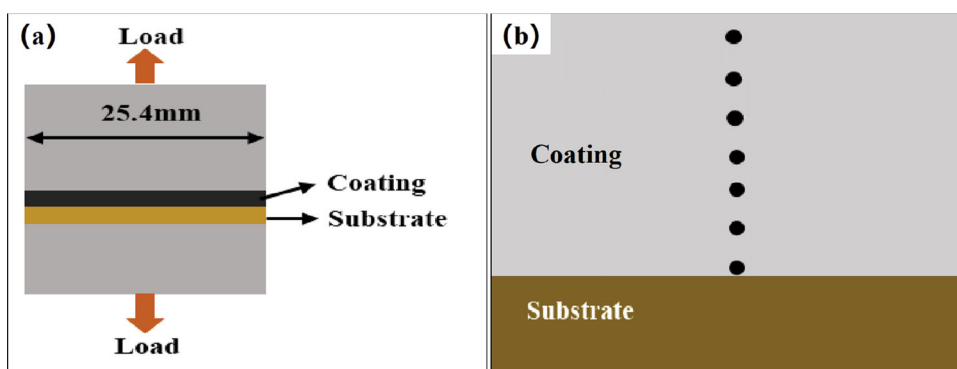
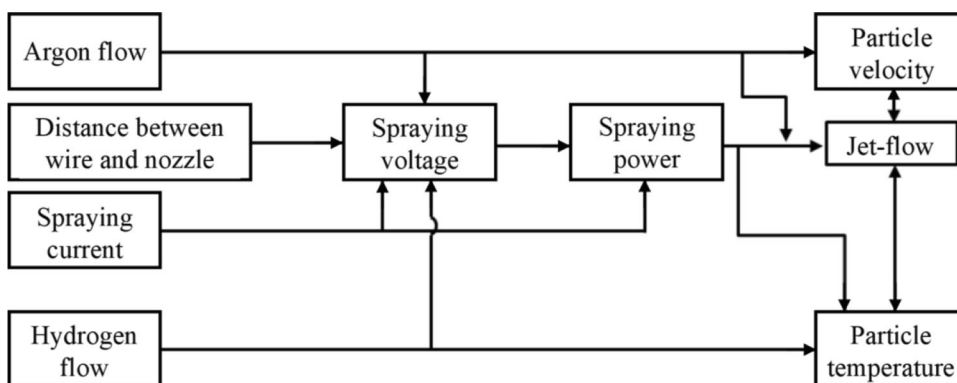


Fig. 7 Relationship between various factors and jet state of plasma transfer arc wire spraying



(4) I influences U and the spraying power.

As for the above-mentioned five factors, only U cannot be manually adjusted, the other four factors can be set during the experiment. Therefore, the influences of L_{Ar} , d , I and L_{H2} on U and jet divergence of PTWAS were mainly analyzed in this paper. In addition, due to the low melting point of Al, according to the preliminary experimental research results of the research group, the spraying current used in this experiment is 120A-200A.

Results and Discussion

Jet Characteristics of PTWAS by Single Factor Method

When exploring, the method of controlling variables is adopted, which only changes one variable that needs to be studied while keeping the other variables unchanged. It is worth noting that the parameters used in the experiment are the most favorable process parameters for coating preparation after a large number of experiments, namely argon gas flow rate of 120 L min^{-1} , spray current of 160 A, hydrogen gas flow rate of 6 L min^{-1} , wire feeding speed of 0.18 m s^{-1} , and distance between wire and nozzle of 10 mm. Therefore, in this section of the experiment, only

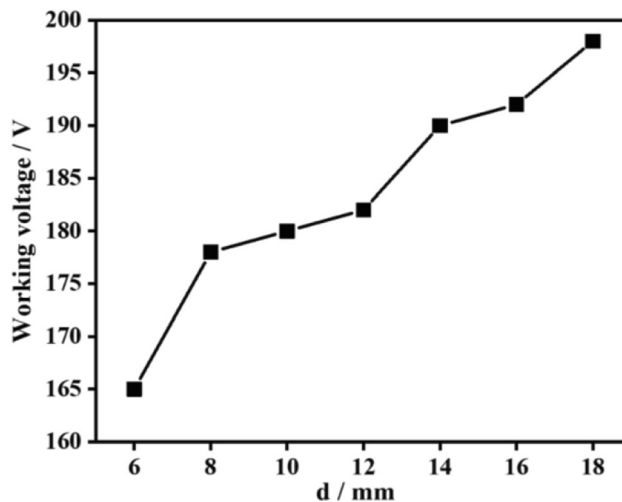


Fig. 8 Effect of distance between wire and nozzle on spray voltage

when studying a single variable, the variables that need to be changed will be changed.

Influences of Various Factors on U

Figure 8 shows the effect of the distance between the wire and the nozzle (d) on the spraying voltage (U), in which L_{Ar} was 120 L min^{-1} , I was 160 A, L_{H2} was 6 L min^{-1} , and V was 0.18 m s^{-1} . It could be seen from Fig. 8 that

U increased gradually with d . The analysis showed that the main reason was that the wire was connected to the large power anode, so the plasma transfer arc was generated between the wire and the nozzle, so the distance between the two was equivalent to the resistance, so d would directly affect U .

When d was increased, the resistance between them was increased, so U gradually increased. It could be seen from Fig. 8 that when d was between 8 and 12 mm, U increased slightly; after 12 mm, U increased sharply with the increase in d .

It was well known that the volt–ampere characteristic of plasma transfer arc was the relationship between I and U , as shown in Fig. 9. It could be found that when other variables were kept constant during the spraying process, L_{Ar} was 120 L min^{-1} , L_{H_2} was 6 L min^{-1} , V was 0.18 m s^{-1} , and d was 10 mm, U gradually increased with the increase in I , and the increase in U slowed down when I was greater than 140 A.

In addition, it was found in the experiment that I should not be too large when V was constant; otherwise, the arc breaking occurred. The spraying power gradually increased with the increase in I , and the wire tip moved in the opposite direction of wire feeding when V was constant, leading to the excessive anode offset and the disappearance of the plasma arc.

Further, we had studied the effect of L_{Ar} on U , as shown in Fig. 10. During the spraying process, I was 160 A, L_{H_2} was 6 L min^{-1} , V was 0.18 m s^{-1} , and d was 10 mm.

Through the analysis of Fig. 10, it was found that U gradually increased with the increase in L_{Ar} , and when L_{Ar} was greater than 120 L min^{-1} , the increase in U became slow. At the same time, during the experiment, it was found that when L_{Ar} was too large, U fluctuated greatly. The analysis showed that the main reason for the above

changes was that with the increase in L_{Ar} , the content of ionized gas in the nozzle channel increased, and the better the acceleration effect of plasma jet would make the anode wire move along the jet direction, thus increasing U ; however, when L_{Ar} was too large, the anode wire would swing back and forth in the jet direction, causing U to fluctuate within a certain range.

It was found that if only argon was selected as the working gas during the spraying process, the melting effect of the cored wire was not ideal, so hydrogen must be added as the auxiliary gas. This was because hydrogen was a diatomic molecule with a high enthalpy value. When ionized, it would release a lot of heat energy, which could make spraying materials with high melting point achieve good melting effect.

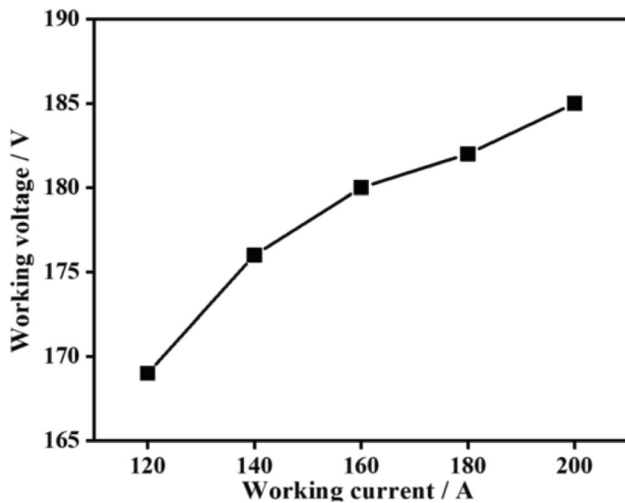


Fig. 9 Effect of spraying current on spraying voltage

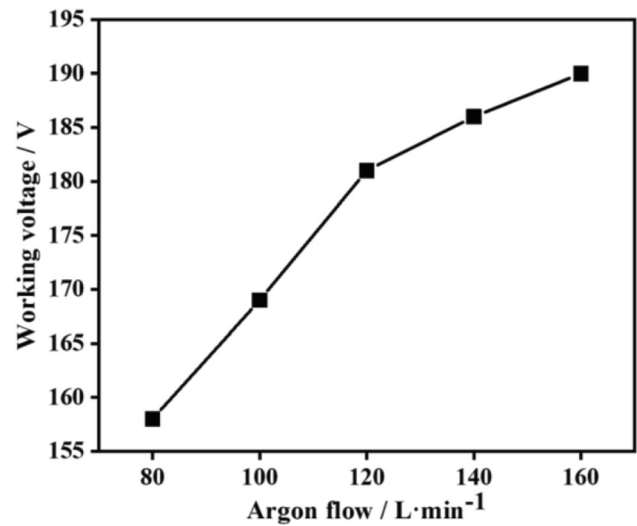


Fig. 10 Effect of argon flow on spray voltage

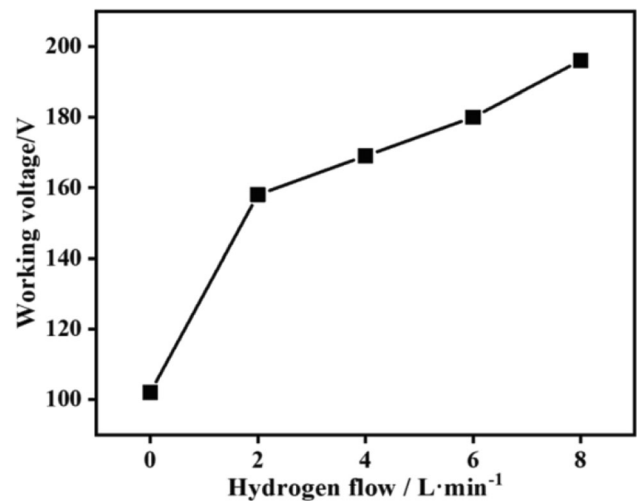


Fig. 11 Effect of hydrogen flow on spray voltage

Figure 11 shows the effect of L_{H_2} on U . During the spraying process, L_{Ar} was 120 L min^{-1} , I was 160 A , V was 0.18 m s^{-1} , and d was 10 mm . It could be found that when hydrogen was not added, U was about 100 V ; When hydrogen was added, U increased rapidly. The analysis showed that this was because after adding hydrogen, a large amount of heat would be released during ionization, which would rapidly increase the temperature and speed of the plasma jet, causing the wire tip to move forward, thus increasing U .

Influences of Various Factors on Jet Divergence

Figure 12 shows the macro-picture of the jet obtained when adjusting the distance between the Al/SiC powder-cored wire and the nozzle. During the spraying process, L_{Ar} was 120 L min^{-1} , I was 160 A , L_{H_2} was 6 L min^{-1} , and V was 0.18 m s^{-1} .

From the figure, it could be observed that as the distance between the powder-cored wire and the nozzle increases, the degree of jet divergence first decreased and then increased. When the distance between the wire and the nozzle was 14 mm (Fig. 12d), the jet diverged abnormally. When the distance between the wire and the nozzle was less than 10 mm , the color of the jet turned white and bright, indicating that the wire was fully melted at this time; However, when the distance was greater than 10 mm , the jet color gradually turned yellow and dark, indicating

that the wire material was not fully melted at this time. The main reason was that as the distance between the two increases, the thermal energy at the position of the wire material decreases, resulting in the wire material not being fully melted.

In order to further study the effect of spraying current on jet divergence. During the spraying, L_{Ar} was 120 L min^{-1} , L_{H_2} was 6 L min^{-1} , V was 0.18 m s^{-1} , and d was 10 mm . The jet photos were taken under different parameter combinations, as shown in Fig. 13.

It could be seen from the figure that when I was 140 A , the color of the jet was dim. The analysis showed that the jet was dim because the spraying power was small, and only part of the wire was melted, resulting in less molten particles; With the increase in I , the jet became white and bright gradually, indicating that with the increase in I , the melting effect of wire was getting better and better. However, in the experiment, when I exceeded 200 A , the divergence of the jet is too large which was no longer suitable for the preparation of the coating. This was due to the excessive melting of the wire and the serious divergence of the molten particles under the action of the high-speed air flow.

Figure 14 shows the macro-photos of the jet under different argon flow rates. During the spraying process, I was 160 A , L_{H_2} was 6 L min^{-1} , V was 0.18 m s^{-1} , and d was 10 mm . It could be seen from the figure that the divergence degree of the jet gradually decreases with the increase in

Fig. 12 Effect of distance between wire and nozzle on jet divergence: (a) 8 mm ; (b) 10 mm ; (c) 12 mm ; (d) 14 mm

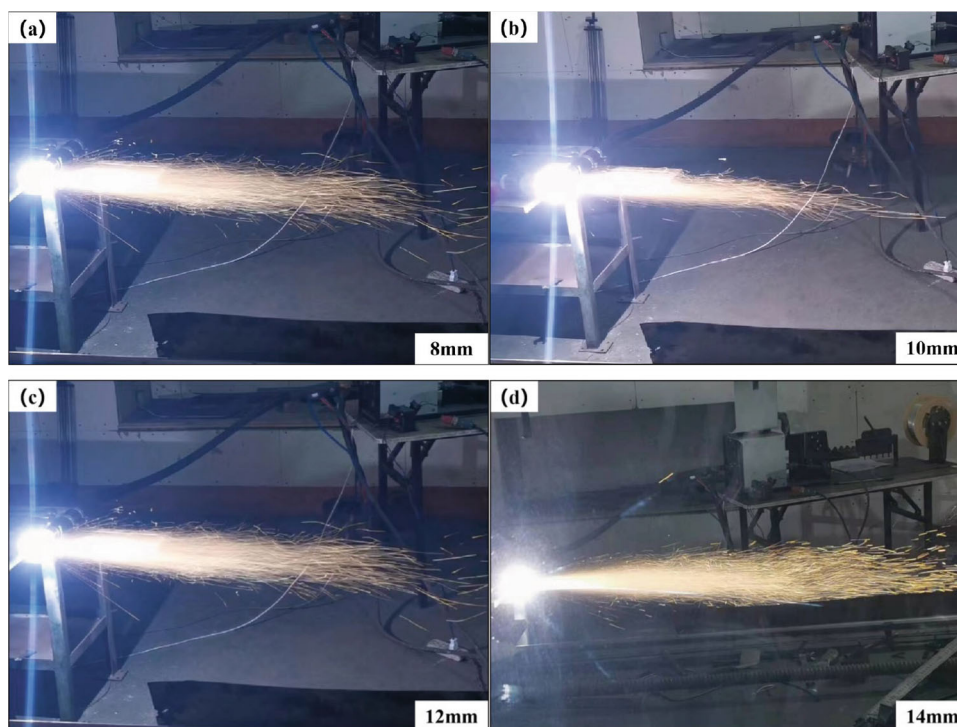


Fig. 13 Effect of spraying current on jet divergence: (a) 140A; (b) 160A; (c) 180A; (d) 200A

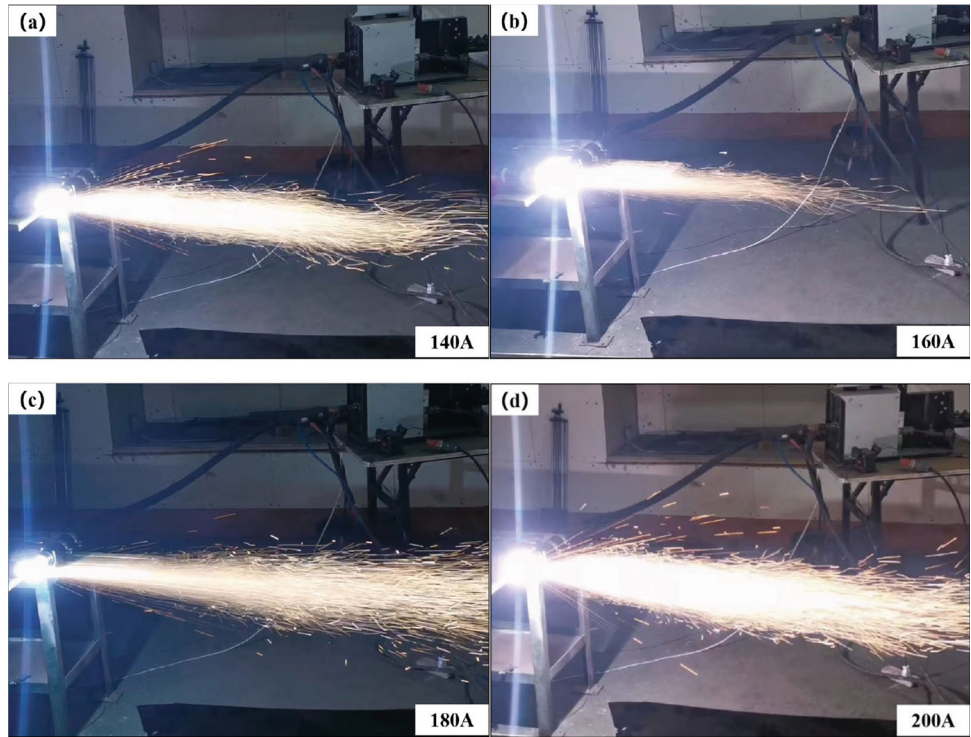
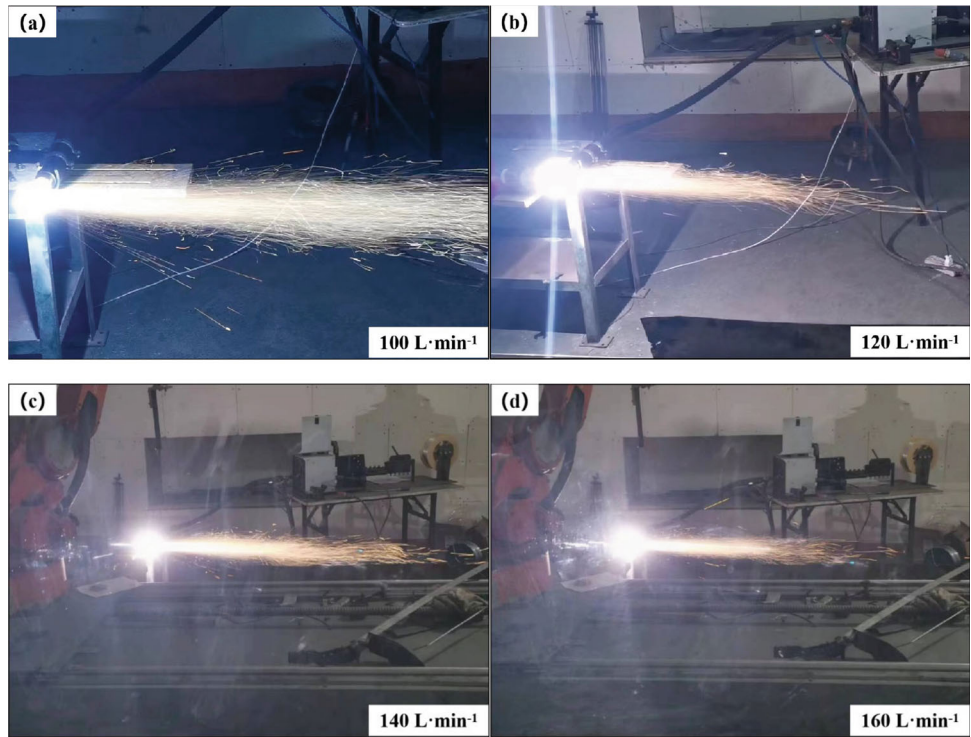


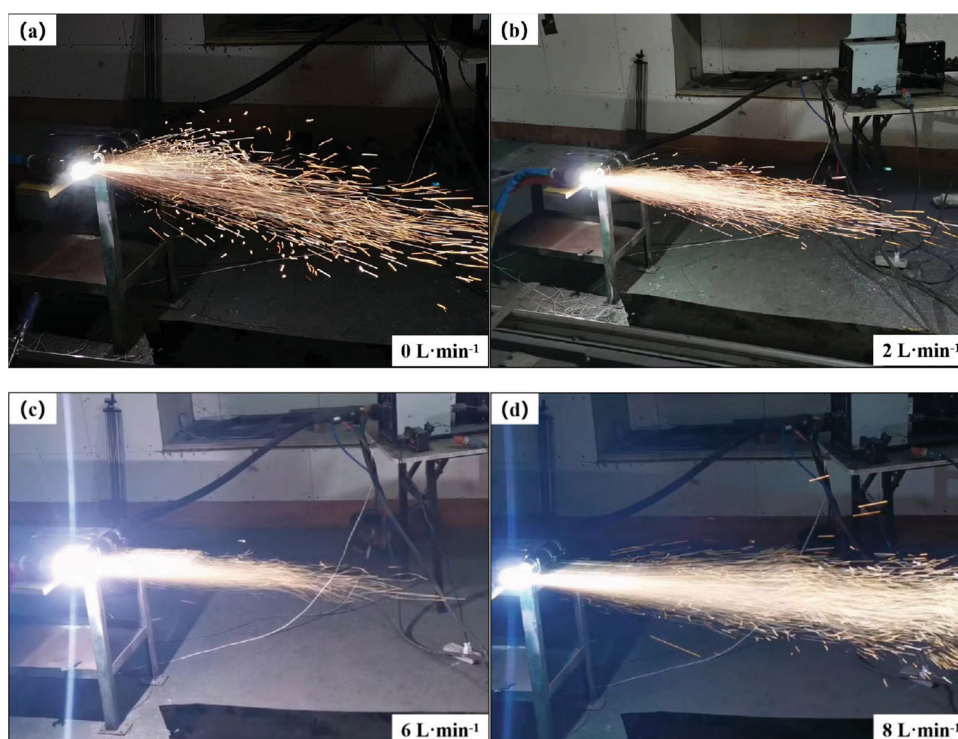
Fig. 14 Effect of argon flow on jet divergence: (a) 100 L min⁻¹; (b) 120 L min⁻¹; (c) 140 L min⁻¹; (d) 160 L min⁻¹



L_{Ar} , and the jet length gradually decreased; at the same time, the color of the jet gradually turned yellow and dark with the increase in L_{Ar} .

The analysis showed that the main reason for the above phenomenon was that with the increase in L_{Ar} , the acceleration effect of compressed gas on particles was more

Fig. 15 Effect of hydrogen flow on jet divergence:
 (a) 0 L min^{-1} ; (b) 2 L min^{-1} ;
 (c) 6 L min^{-1} ; (d) 8 L min^{-1}



obvious, so the particle velocity increased sharply, so the jet divergence degree decreased. However, when L_{Ar} increased, the particles were easier to be cooled and the melting degree of the wire was reduced, so the color of the jet becomes darker.

Finally, in order to study the effect of different L_{H_2} on the jet divergence, in the experiment, keep L_{Ar} was 120 L min^{-1} , I was 160 A , V was 0.18 m s^{-1} , and d was 10 mm , and adjust the hydrogen flow rate, as shown in Fig. 15.

It could be found that when L_{H_2} is 0 L min^{-1} , the divergence of plasma jet was very large, and the jet color was dim. The analysis showed that this was due to the low temperature produced by the plasma arc due to the absence of hydrogen, which led to poor wire melting effect. With the addition of hydrogen, a large amount of heat would be released during the ionization process, so the wire would melt more fully, so the jet would gradually brighten and the divergence degree would gradually decrease. However, when L_{H_2} was 8 L min^{-1} , the divergence degree of the jet increased gradually. The main reason for this phenomenon was that the plasma arc temperature was too high when L_{H_2} was too high, which led to wire over-melting.

Process Parameters of Al-Based Coatings by PTWAS Optimized Through RSM

RSM is an experimental method to solve nonlinear problems, which can achieve the optimal target value by

analyzing the relationship between various influencing factors. Its main process includes experiment design, model building, model verification and result analysis. The models available include the linear model, quadratic model, cubic model and 2FI model, and the fitting function close to the real results can be obtained by verifying each model.

Experiment Design of RSM

Through the analysis in section “[Jet Characteristics Of PTWAS By Single Factor Method](#)”, it was found that the main influencing factors for the preparation of Al/SiC composite coatings by PTWAS included L_{Ar} , L_{H_2} , I , U , V , and d . U was mainly affected by I , L_{Ar} , L_{H_2} , and d and U could not be manually controlled on the operating platform, so the influences of U were ignored.

As demonstrated by the analysis results in section “[Jet Characteristics of PTWAS by Single Factor Method](#)”, the nozzle was easy to burn out when d was too small (less than 8 mm), that is, the wire was too close to the nozzle. In contrast, the melting effect of the wire became worse and the jet got divergent and dark when d was too large (more than 10 mm). Therefore, it was considered that the optimal d was 10 mm , and the other three factors were taken as response factors.

According to Section 3.1.3, the jet began diverging when L_{Ar} was 100 L min^{-1} , which resulted from the low particle velocity, so the minimum L_{Ar} was 100 L min^{-1} .

The jet gradually became dark when L_{Ar} exceeded 140 L min^{-1} , indicating that the wire was not fully melted, so L_{Ar} was between 110 and 130 L min^{-1} . Likewise, the ranges of L_{H2} and I were $4\text{-}8 \text{ L min}^{-1}$ and $140\text{-}180 \text{ A}$, respectively. The final response level is shown in Table 3.

Response Results and Verification

Porosity is an important factor to measure the compactness of the coating. Generally, the lower the porosity is, the better the performance of the coating is. Therefore, the porosity was taken as the response target value, and 17 set of process parameters were designed and optimized using the BBD of Design-E software. For the Al/SiC composite coating obtained by each set of process parameters, the porosity of the sample was calculated by gray scale method, and the results are shown in Table 4. It could be seen from the table that the porosity of the coating prepared with different process parameters changed significantly, indicating that the optimized combination of L_{Ar} , I and L_{H2} could produce excellent Al/SiC composite coating.

Table 3 Response factor level table

Response factors	- 1	0	1
$L_{Ar}/L, \text{ min}^{-1}$	110	120	130
$L_{H2}/L, \text{ min}^{-1}$	4	6	8
I/A	140	160	180

Table 4 Response surface test results

Experiment no.	$L_{Ar}/L, \text{ min}^{-1}$	$L_{H2}/L, \text{ min}^{-1}$	I/A	Porosity, %
1	110	8	160	6.1
2	110	6	140	5.9
3	120	6	160	1.9
4	120	6	160	2.3
5	130	4	160	3.1
6	130	6	180	4.5
7	120	8	140	8.9
8	110	4	180	10.8
9	120	4	140	3.5
10	120	6	160	1.9
11	120	6	160	1.6
12	110	4	160	6.8
13	110	6	180	8.2
14	120	6	160	1.3
15	130	6	140	8.9
16	120	8	180	4.3
17	130	8	180	5.7

Table 5 shows the experimental results obtained from four fitting models. It was found that the quadratic model had the smallest sequential P value (< 0.0001), which indicated that the quadratic model was the most significant, so the fitting results of the quadratic model were selected in the follow-up experiments.

According to the quadratic model, the relationship equation among the three factors (L_{Ar} , I and L_{H2}) and porosity (Eq 1) is as follows:

$$\begin{aligned} \text{Porosity} = & 1.87 - 0.78 \times I - 0.40 \times L_{Ar} + 1.02 \times L_{H2} \\ & - 1.67 \times I \times L_{Ar} \\ & - 1.52 \times I \times L_{H2} + 1.40 \times L_{H2} \times L_{Ar} + 2.02 \\ & \times I^2 + 2.86 \times L_{Ar}^2 + 1.41 \times L_{H2}^2 \end{aligned} \tag{Eq 1}$$

According to the coefficients of the fitting equation, among the three influencing factors, L_{H2} had the most significant influence on coating porosity, while L_{Ar} had little influence on coating porosity. In terms of the common influences of the two, $L_{Ar}\text{-}I$ had the largest influence on the coating porosity, while $L_{H2}\text{-}L_{Ar}$ had the smallest influence.

Table 6 displays the variance analysis results of the quadratic model of porosity. It was found that the F value of the quadratic model of porosity was 49.40, and the P value was less than 0.0001, manifesting that the regression equation of porosity and L_{Ar} , L_{H2} and I of the coating under the quadratic model fit well. In addition, the misfit degree of the P value and F value was 0.1387 and 3.31, respectively, meaning that the error between the fitted value and the actual value was small and the fitting result was accurate. It should be noted that F -value is an indicator in analysis of variance, which generally compares differences between groups. The larger the F value, the smaller the P value, indicating a more reliable result. The F -value represents the significance of the entire fitting equation. The larger the F -value, the more significant the equation is and the better the fitting degree is. The P value is an indicator of the difference between the control group and the experimental group.

In the model, L_{H2} has the smallest P value, indicating that L_{H2} has the most significant impact on porosity; The

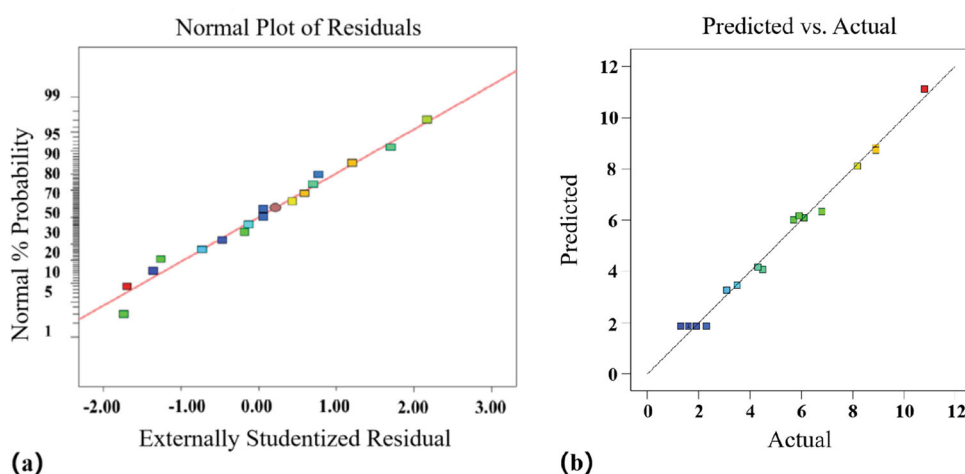
Table 5 Response surface fitting model

Model	Sequential (P value)	Lack of fit (P value)
Linear model	0.6882	0.0005
Quadratic model	< 0.0001	0.1389
2FI model	0.1794	0.0006
Cubic model	0.1389	

Table 6 Results of variance analysis of porosity quadratic model

	Sum of variances	D_f	Mean variance	F-value	P value	
Model	141.11	9	6.31	39.79	< 0.0001	Remarkable
I	4.12	1	4.12	10.44	0.0144	
L_{Ar}	1.19	1	1.19	3.01	0.1263	
L_{H2}	6.00	1	6.00	15.23	0.0059	
$I-L_{Ar}$	12.19	1	12.19	30.93	0.0008	
$I-L_{H2}$	8.47	1	8.47	21.49	0.0024	
$L_{Ar}-L_{H2}$	6.77	1	6.77	17.18	0.0043	
I^2	11.73	1	11.73	29.76	0.0010	
L_{Ar}^2	24.87	1	24.87	63.12	< 0.0001	
L_{H2}^2	7.72	1	7.72	19.59	0.0031	
Lack of fit	1.97	3	0.66	3.31	0.1389	Not significant

Fig. 16 The normal plot of residuals of Al/SiC coatings and the relationship between predicted and actual: (a) normal plot of residuals; (b) predicted vs. actual



P value of I in the model is centered, indicating that I has a secondary impact on porosity; The P value of L_{Ar} in the model is the highest, indicating that the effect of L_{Ar} on the porosity of the coating is the least significant. In the interaction among the three factors, the P value of $I-L_{Ar}$ in the model is the smallest, indicating that $I-L_{Ar}$ has the most significant impact on porosity; The P value of $I-L_{H2}$ in the model is in the middle, indicating that $I-L_{H2}$ has a secondary impact on porosity; The maximum value of $L_{Ar}-L_{H2}$ in the model indicates that the influence of $L_{Ar}-L_{H2}$ on porosity is not significant, and the above results are consistent with the analysis of the quadratic fitting equation.

As is well known, when all points in the residual normal distribution map are near a straight line, it indicates that the model is suitable; when the points in the residual and predicted value relationship graph are scattered, it can further indicate that the model is suitable. The residual normal distribution of the model is shown in Fig. 16(a), and it can be observed that the residual distribution of the fitted model is roughly on the same straight line, indicating that the deviation between the predicted and true values of

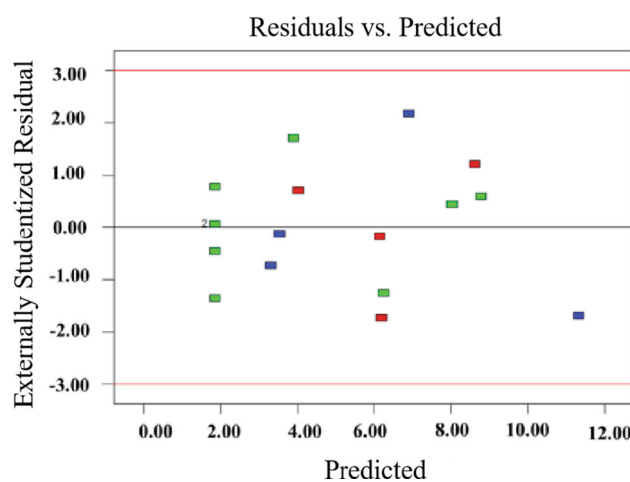
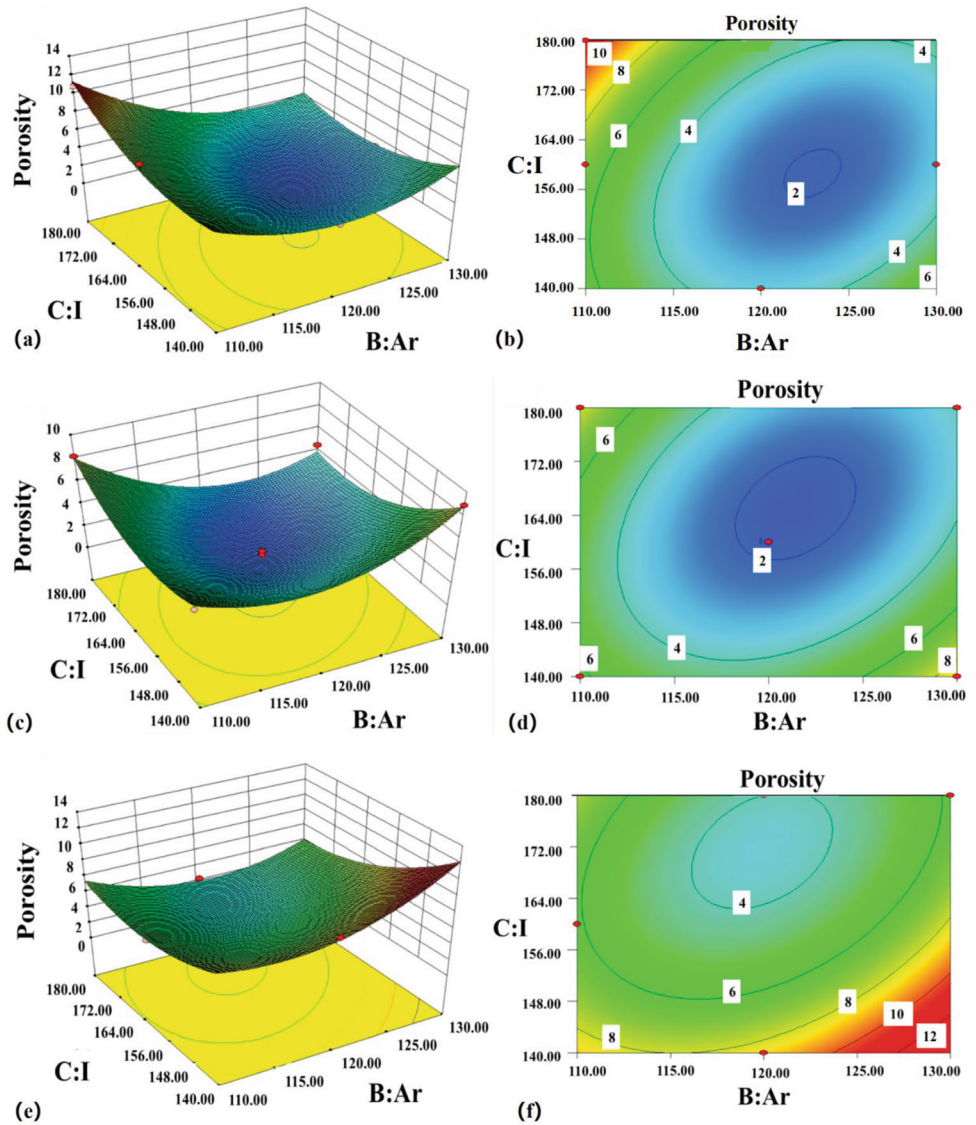


Fig. 17 Residual and predicted value distribution of porosity of Al/SiC composite coating

porosity is very small (Fig. 16b). Figure 17 shows the relationship between residuals and predicted values. It can be observed that residuals are randomly distributed and

Fig. 18 Effect of I and L_{Ar} on porosity of Al/SiC composite coating under different L_{H2} : (a-b) L_{H2} is 4 L min^{-1} , 3D surface relationship and contour of I , L_{Ar} and Porosity; (c-d) L_{H2} is 6 L min^{-1} , 3D surface relationship and contour of I , L_{Ar} and Porosity; (e-f) L_{H2} is 8 L min^{-1} , 3D surface relationship and contour of I , L_{Ar} and Porosity



irregular in the attachment of “0”, further indicating that the quadratic model can be used to fit the relationship between porosity and various factors.

Response Surface Analysis

According to the analysis results in section “[Response Results and Verification](#)”, among single factors, L_{H2} had the most significant influence on the coating porosity, while in the interaction, $I-L_{Ar}$ had the most significant influence on the coating porosity. Therefore, the interaction of $I-L_{Ar}$ on the porosity of Al/SiC composite coatings at different L_{H2} could be further analyzed through the response surface diagram, as shown in Fig. 18.

It was observed from the figure that when L_{Ar} and I were kept constant, the porosity decreased first and then

increased with the increase in L_{H2} , and the main reasons are as follows:

- (1) When L_{H2} is too small, the enthalpy and the temperature of the plasma jet are low, and the wire is not fully melted. Besides, there are semi-melted and unmelted particles. When these particles are deposited in the coatings, the pores and defects will increase, undermining the compactness of the coatings.
- (2) As L_{H2} increases, the enthalpy and the temperature of the plasma jet also increase. Meanwhile, the melting effect of the wire is better. Specifically, the number of semi-melted and unmelted particles decreases, more particles uniformly spread on the substrates, the coating quality is higher, and the pores and defects are reduced.

- (3) When L_{H2} is too large, the wire is in an over-melted state, the in-flight velocity of particles decreases, and the particle beams diverge, which will lead to the longer residence time of molten Al droplets in the jet and aggravate the oxidation of Al. Meanwhile, the particle velocity is low, and the particles are not fully spread on the substrates, and the porosity of the coatings will accordingly increase.

When L_{H2} is kept constant, the interaction of L_{Ar} and I on the porosity of composite coatings lies in that the porosity decreases first and then increases with the increase in L_{Ar} and I . The main reasons are as follows:

- (1) As L_{Ar} increases, the working gas inside the spray gun increases, the acceleration effect of the plasma arc formed in the nozzle on particles becomes more significant, the in-flight velocity of the particles increases, and the particles spread more fully on the substrates. Meanwhile, the cooling effect on particles becomes more significant with the increase in L_{Ar} , which undermines the melting degree of particles.
- (2) As I increases, the spraying power increases, and the melting effect of particles gradually becomes better. However, when I is too large, the plasma jet becomes divergent.

In addition, it was found from the figure that when I decreased and L_{Ar} increased simultaneously or I increased and L_{Ar} decreased, the coating porosity was very high. For example, the porosity was 8.9% when L_{Ar} was 130 L min^{-1} , L_{H2} was 6 L min^{-1} and I was 140 A. The porosity was 8.2% when L_{Ar} was 110 L min^{-1} , L_{H2} was 6 L min^{-1} and I was 180 A. The analysis revealed that the increase in L_{Ar} resulted in the increase in particle velocity and the decrease in the melting degree of particles, and meanwhile, the decrease in I led to the reduced melting degree of particles, so the coating porosity was very high.

To sum up, the optimal process parameters for preparing Al/SiC composite coatings by PTWAS based on RSM are as follows: L_{Ar} was 120 L min^{-1} , I was 160 A, L_{H2} was

5 L min^{-1} , spraying distance was 100 mm, V was $0.18 \text{ m}\cdot\text{s}^{-1}$, and d was 10 mm.

Microstructure and Mechanical Properties of Al/SiC Composite Coatings

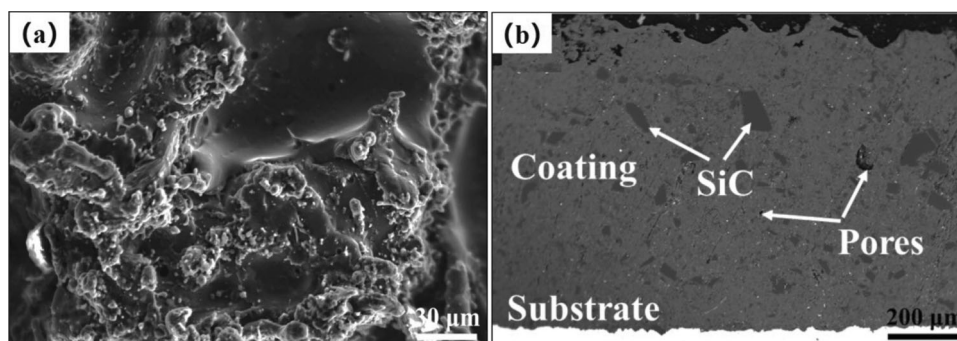
Figure 19 shows the surface and cross-sectional morphology of Al/SiC composite coatings prepared by the optimized spraying process (Table 7). It was found that compact and uniform coatings were prepared on the surfaces of 304 stainless steel substrates by PTWAS, and both coatings bonded well with the substrates without cracks or delamination. It was observed on the coating surface that there were few pores on the surfaces of Al/SiC composite coatings (Fig. 19b), but there were still a few pits, which might result from the SiC particles impacting the Al coatings. In addition, a few pores were observed in the cross sections of the coatings. The analysis showed that the metal droplets spread well on the surfaces of the substrates during the coating deposition, but there were a few pores in the coatings due to layer-by-layer accumulation and insufficient spread of partial droplets. Moreover, it was found that SiC particles were embedded in Al coatings to form a composite framework (Fig. 19b).

The SEM morphology and corresponding element distribution of Al/SiC composite coating are shown in Fig. 20. It can be observed that both Al and O elements are uniformly distributed in the two coatings, and SiC particles have good bonding with Al, with no obvious cracks at the

Table 7 Spraying parameters used for deposition of the coatings

Spraying parameters	Numerical value
Argon flow	120 L min^{-1}
Hydrogen flow	5 L min^{-1}
Spraying current	160 A
Spraying distance	100 mm
Distance between wire and nozzle	10 mm
Wire feeding speed	0.18 m s^{-1}

Fig. 19 Micro morphology of Al/SiC composite coating: (a) surface morphology; (b) section morphology



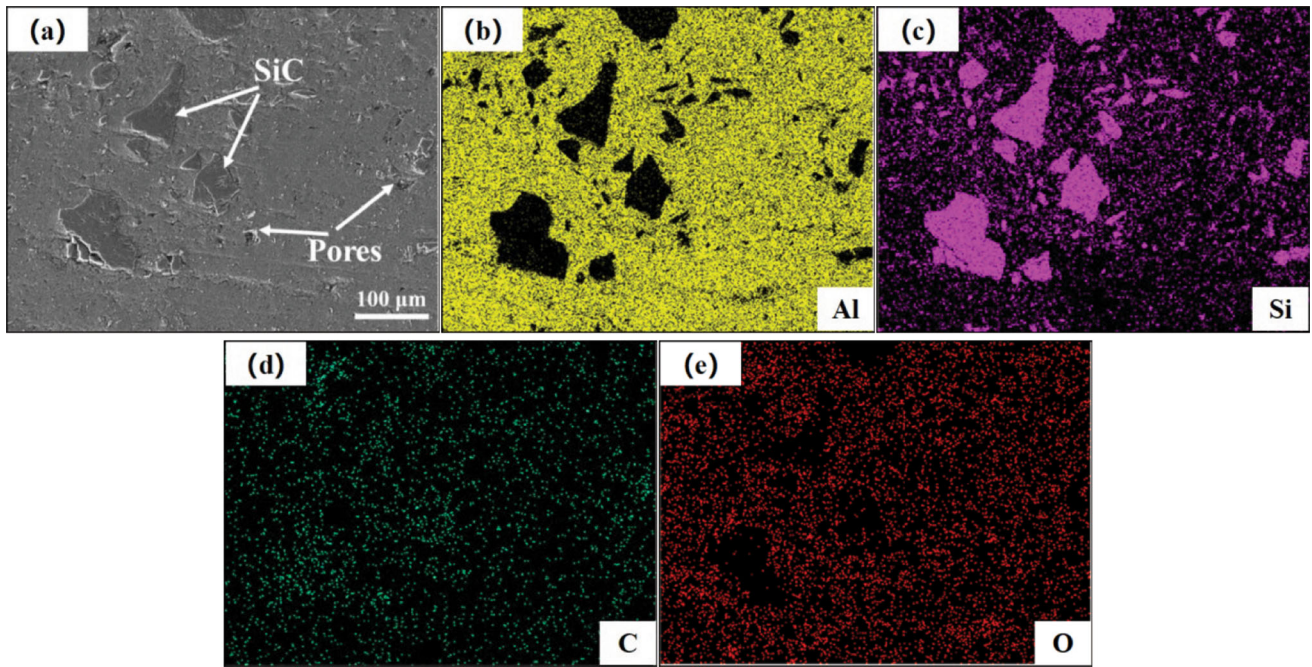


Fig. 20 SEM morphology and element distribution diagram of Al/SiC composite coating: (a) SEM morphology; (b) Al element; (c) Si element; (d) C element; (e) O element

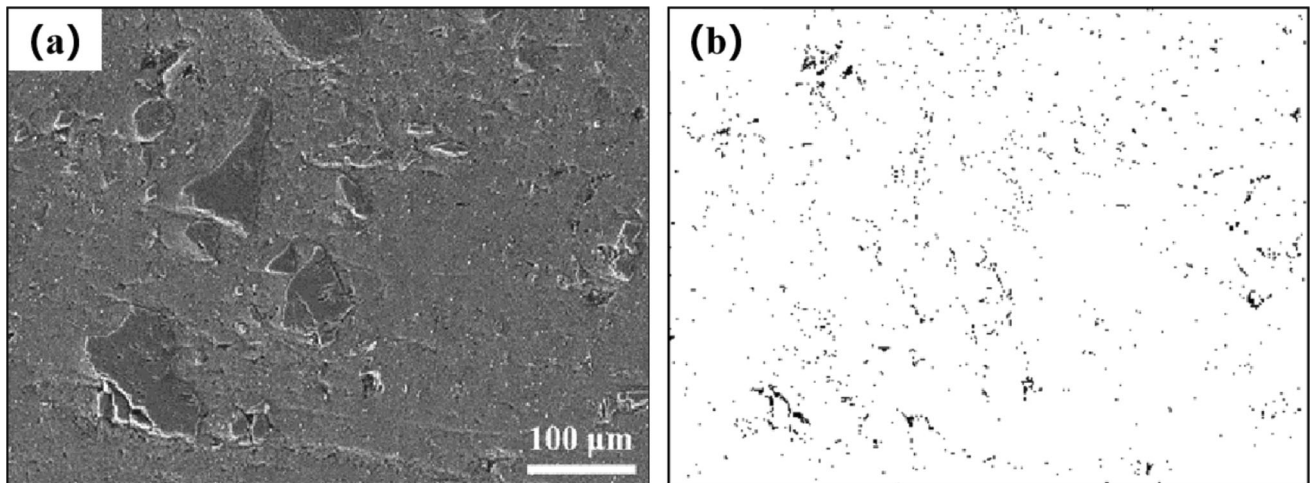


Fig. 21 Pore statistics of Al/SiC composite coatings: (a) SEM images; (b) corresponding pore grayscale map

interface junction. It should be noted that the distribution of C element shown in Fig. 20d is not entirely the actual distribution of C element in the coating sample, but rather serves as a reference. However, the approximate distribution of C element can still be distinguished from Fig. 20d, as the reference element used for EDS scanning in this experiment is C.

Further processing of the cross-sectional morphology of the coating using ImageJ2x software resulted in a grayscale image of the pores in the coating (Fig. 21b). From the figure, it can be seen that there are no large pores or cracks

in the Al/SiC composite coating, and the coating is relatively dense. Further statistical data analysis shows that the average porosity of Al/SiC composite coatings is only 1.6%.

Figure 22 demonstrates the Vickers hardness of the Al/SiC composite coatings at different positions from the substrates and five sets of bonding strength test data. It was found that the hardness of Al/SiC composite coatings fluctuated a lot, and the highest hardness reached 140 HV_{0.1}. The average microhardness of Al/SiC composite coatings was calculated to be 102 HV_{0.1}, and the average

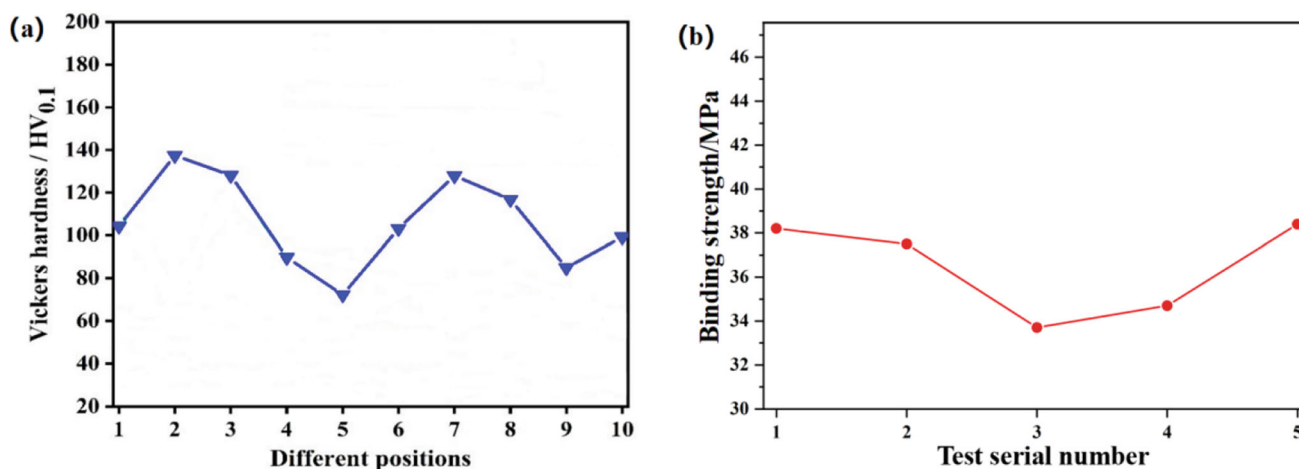


Fig. 22 (a) Vickers hardness of Al/SiC composite coating at different positions from the substrate; (b) 5 groups of bonding strength test values

bonding strength was 36.5 MPa, indicating a better bonding effect than that of the Al/SiC composite coatings by WFS (Ref 34).

Conclusion

In this paper, the PTWAS technology was innovatively developed to spray Al/SiC powder-cored wires, and Al/SiC composite coatings with excellent properties were prepared. In this research, the influences of different parameters on the U and jet characteristics of Al/SiC powder-cored wires by PTWAS were mainly studied, and the interaction of L_{Ar} , L_{H2} , I and d on the porosity of Al/SiC composite coatings was analyzed through RSM. On this basis, the coating preparation process parameters were optimized. The main conclusions obtained are as follows:

- (1) U increased with the increase in d , and so did the jet divergence. The jet was bright and the particles melted well when d was less than 10 mm, while the plasma jet became dark and the melting of particles was undermined when d was greater than 10 mm.
- (2) U gradually increased and the jet became shorter and darker with the increase in L_{Ar} . U increased, the jet became bright, and the particles gradually melted well with the increase in L_{H2} .
- (3) As I increased, U gradually increased with a small changing range, and I should not exceed 200 A; otherwise, the jet would abnormally diverge.
- (4) Through the quadratic model fitting, the influences of L_{Ar} , L_{H2} , and I on the porosity of Al/SiC composite coatings are as follows: $L_{H2} > I > L_{Ar}$. The interaction of the three factors on the porosity of composite coatings is as follows: $L_{Ar}-I > I-L_{H2} > L_{Ar}-L_{H2}$. The optimal process parameters for

preparing Al/SiC composite coatings by PTWAS technology through RSM were obtained as follows: L_{Ar} was 120 L min^{-1} , I was 160 A, L_{H2} was 5 L min^{-1} , spraying distance was 100 mm, V was 0.18 m s^{-1} , and d was 10 mm.

- (5) The porosity of the Al/SiC composite coatings prepared by optimized process parameters was reduced to 1.6%, the average microhardness reached 102 HV_{0.1}, and the average bonding strength reached 36.5 MPa.

Acknowledgments This work was supported by the National Natural Science Foundation of China (Grant No. 52105235, 52075542 and 52130509) and 145 Project.

References

1. S. Kamal, R. Jayaganthan, and S. Prakash, Evaluation of Cyclic Hot Corrosion Behaviour of Detonation Gun Sprayed Cr₃C₂-25 %NiCr Coatings on Nickel- and Iron-Based Superalloys, *Surf. Coat. Technol.*, 2009, **203**(8), p 1004-1013.
2. H.J. Wang, Guide for thermal spraying engineers [M]. *National defense industry press*, 2010.
3. J. Li, The Study on Application and Development of Thermal Spray Technology [D]. *Jilin University*, 2015.
4. P. Frank, S. Jochen, and K. Zhang, Thermal Spraying of Zinc and Zinc-Aluminium Corrosion Protection, *Therm. Spray Technol.*, 2012, **4**(03), p 71-75.
5. J.Q. Zhou, S. Qin, X.B. Min et al., Research on Performance of Thermal Spraying Zn Coating, *Metal Mater. Metall. Eng.*, 2016, **44**(01), p 13-19+57.
6. V.C. Silva and R.S. Paredes, Effect of Preheating and of Single and Multiple Passes on the Porosity, Oxidation and Microhardness of a Duplex Stainless Steel Coating Deposited by Wire Flame Thermal Spraying, *Weld. Int.*, 2018, **32**(8), p 550-560.
7. S. Yin, X.F. Wang, W.Y. Li et al., Deformation Behavior of the Oxide Film on the Surface of Cold Sprayed Powder Particle, *Appl. Surf. Sci.*, 2012, **259**, p 294-300.

8. V. Sharma, S. Kumar, M. Kumar et al., High Temperature Oxidation Performance of Ni-Cr-Ti and Ni-5Al Coatings, *Mater. Today Proc.*, 2020, **26**, p 3397-3406.
9. Y. Zhou, Y.D. Liu, X.L. Ma et al., Microstructure and Anti-corrosion Properties of Arc-Sprayed Zn-Al-Mg Coating, *Hot Work. Technol.*, 2016, **45**(12), p 138-141.
10. R.A. Haraga, D.L. Chicet, N. Cimpoiu et al., Influence of the Stand-Off Distance and of the Layers Thickness on the Adhesion and Porosity of the 97MXC Deposits Obtained by Arc Spraying Process, *IOP Conf. Ser. Mater. Sci. Eng.*, 2020, **877**, p 012020.
11. C.J. Li, Applications, Research Progresses and Future Challenges of Thermal Spray Technology, *Therm. Spray Technol.*, 2018, **10**(04), p 1-22.
12. M. Wang, Microstructure and Properties of FeAlNbB Coating By Arc Spraying [D]. *Xi'an Shiyou University*, 2018.
13. J.R. Baughman, D.J. Cook, D.R. Marantz, et al. Plasma transferred wire arc thermal spray apparatus and method [P]. *US*, 1999.
14. A. Edrissy, T. Perry, Y.T. Cheng et al., Wear of Thermal Spray Deposited Low Carbon Steel Coatings on Aluminum Alloys, *Wear*, 2001, **251**, p 1023-1033.
15. K. Bobzin, F. Ernstf, K. Richardt et al., Thermal Spraying of Cylinder Bores with the Plasma Transferred Wire Arc Process, *Surf. Coat. Technol.*, 2008, **202**(18), p 4438-4443.
16. S. Devaraj, B. Anand, M. Gibbons et al., Thermal Spray Deposition of Aluminum and Zinc Coatings on Thermoplastics, *Surf. Coat. Technol.*, 2020, **399**, p 126114.
17. S. Ghaziof and W. Gao, Electrodeposition of Single Gamma Phased Zn-Ni Alloy Coatings from Additive-Free Acidic Bath, *Appl. Surf. Sci.*, 2014, **311**, p 635-642.
18. L.B. Huang, S.F. Yu, Y. Deng et al., Research Progress and Application of Arc Spraying Cored Wires, *Mater. Rev.*, 2011, **25**(03), p 63-65.
19. P. Daram, P.R. Munroe, and C. Banjongprasert, Microstructural Evolution and Nanoindentation of NiCrMoAl Alloy Coating Deposited by Arc Spraying, *Surf. Coat. Technol.*, 2020, **391**, p 125565.
20. H.L. Tian, C.L. Wang, M.Q. Guo et al., Phase Composition and Formation Mechanisms of a High-Velocity Electric Arc-Sprayed FeNiCrAl Coating, *J. Alloys Compd.*, 2018, **769**, p 998-1006.
21. Z.X. Zhu, D. Chen, and B.S. Xu, Effect of RE on Microstructure and Electrochemical Corrosion Behavior of Arc Sprayed Zn-Al-Mg Coating, *Appl. Mech. Mater.*, 2011, **66-68**, p 727-730.
22. M.Y. Kharlamov, I.V. Krivtsun, and V.N. Korzhyk, Dynamic Model of the Wire Dispersion Process in Plasma-Arc Spraying, *J. Therm. Spray Technol.*, 2014, **23**, p 420-430.
23. I.P. Gulyaev, A.V. Dolmatov, M.Y. Kharlamov et al., Arc-Plasma Wire Spraying: An Optical Study of Process Phenomenology, *J. Therm. Spray Technol.*, 2015, **24**, p 1566-1573.
24. M.Y. Kharlamov, I.V. Krivtsun, V.N. Korzhyk et al., Formation of Liquid Metal Film at the Tip of Wire-Anode in Plasma-Arc Spraying, *Paton Weld. J.*, 2011, **12**, p 2-6.
25. A.V. Dolmatov, I.P. Gulyaev, V.I. Kuzmin et al., Analysis and Optimization of Gas-Thermal Spray Process in Terms of Condensed Phase Velocity and Temperature, *Thermophys. Aeromech.*, 2017, **24**, p 83-94.
26. M.Y. Kharlamov, I.V. Krivtsun, V.N. Korzhyk et al., Heating and Melting of Anode Wire in Plasma arc Spraying, *Paton Weld. J.*, 2011, **5**, p 2-7.
27. Q.J. Zhu, K. Wang, X.H. Wang et al., Electrochemical Impedance Spectroscopy Analysis of Cold Sprayed and Arc Sprayed Aluminium Coatings Serviced in Marine Environment, *Surf. Eng.*, 2012, **28**(4), p 300-305.
28. E.A. Esfahani, H. Salimijazi, M.A. Golozar et al., Study of Corrosion Behavior of Arc Sprayed Aluminum Coating on Mild Steel, *J. Therm. Spray Technol.*, 2012, **21**(6), p 1195-1202.
29. X.Y. Chen, J.H. Yuan, J. Huang et al., Large-Scale Fabrication of Superhydrophobic Polyurethane/Nano-Al₂O₃ Coatings by Suspension Flame Spraying for Anti-corrosion Applications, *Appl. Surf. Sci.*, 2014, **311**, p 864-869.
30. B. Syrek-Gerstenkorn, S. Paul, and A.J. Davenport, Use of Thermally Sprayed Aluminium (TSA) Coatings to Protect Off-shore Structures in Submerged and Splash Zones, *Surf. Coat. Technol.*, 2019, **374**, p 124-133.
31. K. Sadashivappa and R.N. Marigoudar, Dry Sliding Wear Behaviour of SiC Particles Reinforced Zinc-Aluminium (ZA43) Alloy Metal Matrix Composites, *J. Miner. Mater. Charact. Eng.*, 2011, **10**(5), p 419-425.
32. R. Arrabal, A. Pardo, M.C. Merino et al., Al/SiC Thermal Spray Coatings for Corrosion Protection of Mg-Al Alloys in Humid and Saline Environments, *Surf. Coat. Technol.*, 2010, **204**(16-17), p 2767-2774.
33. X.W. Peng, G.H. Wang, Z. Zhou et al., Microstructural Features and Properties of Aluminum-based Composite Coatings Containing Ceramic Particles by Arc Spraying, *Therm. Spray Technol.*, 2019, **11**(01), p 63-70.
34. M. Campo, M. Carboneras, M.D. López, B. Torres, P. Rodrigo, E. Otero, and J. Rams, Corrosion Resistance of Thermally Sprayed Al and Al/SiC Coatings on Mg, *Surf. Coat. Technol.*, 2009, **203**(20-21), p 3224-3230.

Publisher's Note Springer Nature remains neutral with regard to jurisdictional claims in published maps and institutional affiliations.

Springer Nature or its licensor (e.g. a society or other partner) holds exclusive rights to this article under a publishing agreement with the author(s) or other rightsholder(s); author self-archiving of the accepted manuscript version of this article is solely governed by the terms of such publishing agreement and applicable law.